Emergence of asymmetric skew-scattering dominated anomalous Nernst effect in the spin gapless semiconductors $Co_{1+x}Fe_{1-x}CrGa$

A. Chanda,[1] Deepika Rani,[2,*] Jadupati Nag,[2] Aftab Alam,[2] K. G. Suresh,[2,†] M. H. Phan,[1,‡] and H. Srikanth[1,§]

[1]*Department of Physics, University of South Florida, Tampa, Florida 33620, USA*

[2]*Magnetic Materials Laboratory, Department of Physics, Indian Institute of Technology Bombay, Mumbai–400076, India*

(Received 17 June 2022; accepted 30 September 2022; published 18 October 2022)

Heusler alloy-based spin gapless semiconductors (SGSs) with very high Curie temperatures (T_C) have recently gained enormous attention because of their unconventional electronic structures. They exhibit a nonzero band gap in one of the spin channels and a zero band gap in the other spin channel, making them an important class of materials for tunable spin transport. Here, we report the experimental observation of anomalous Nernst effect (ANE) in $Co_{1+x}Fe_{1-x}CrGa$ ($x = 0$, 0.2, 0.4, and 0.5), which are the emerging quaternary Heusler alloy-based SGSs. While the electron-electron elastic scattering and the disorder-mediated weak localization effect play the major roles in electrical transport for all the samples at low temperatures, the magnon-drag effect was found to dominate the longitudinal thermoelectric transport. The ANE coefficient at room temperature increases from $\approx 0.018\,\mu V\,K^{-1}$ for $x = 0$ to $\approx 0.063\,\mu V\,K^{-1}$ for $x = 0.5$, which is higher than that for $Ni_{81}Fe_{19}$ and compressively strained $SrRuO_3$ films. Our analysis indicates that the observed ANE in these samples originates from asymmetric skew scattering of charge carriers.

DOI: 10.1103/PhysRevB.106.134416

I. INTRODUCTION

Recent progress in the field of spincaloritronics has stimulated renewal of interest in efficiently harvesting electrical energy from waste thermal energy by exploiting the spin degree of freedom of the charge carriers in a magnetic conductor [1]. The anomalous Nernst effect (ANE) is one of such emerging magnetothermoelectric phenomena, wherein an electrical field ($\overrightarrow{E_{ANE}}$) is generated in a ferromagnetic conductor transverse to the directions of both applied temperature gradient ($\overrightarrow{\nabla T}$) and the magnetization ($\vec{M}$), and can be expressed as, $\overrightarrow{E_{ANE}} = Q_{ANE}(\mu_0 \vec{M} \times \overrightarrow{\nabla T})$, where Q_{ANE} is the coefficient of ANE [2,3]. Berry curvature at the Fermi level associated with the Bloch waves in the reciprocal space ($\vec{k}$ space) has been identified as the underlying intrinsic origin of large room-temperature ANE coefficient observed in a range of topological magnetic materials, e.g., the full-Heusler ferromagnet Co_2MnGa ($\sim 6\,\mu V\,K^{-1}$) [4], magnetic Weyl semimetal $Co_3Sn_2S_2$ ($\sim 5\,\mu V\,K^{-1}$) [5,6], iron-based cubic ferromagnets Fe_3Ga ($\sim 4\,\mu V\,K^{-1}$) and Fe_3Al ($\sim 2\,\mu V\,K^{-1}$) [7], kagome ferromagnets Fe_3Sn ($\sim 3\,\mu V\,K^{-1}$) [8] and Fe_3Sn_2 ($\sim 1.26\,\mu V\,K^{-1}$) [9], chiral antiferromagnet Mn_3Sn ($\sim 0.35\,\mu V\,K^{-1}$) [2], etc., as well as gigantic low-temperature ANE coefficient in correlated noncentrosymmetric kagome ferromagnet $UCo_{0.8}Ru_{0.2}Al$ ($\sim 23\,\mu V\,K^{-1}$) [10], canted antiferromagnet $YbMnBi_2$ ($\sim 6\,\mu V\,K^{-1}$) [11], van der Waals ferromagnet Fe_3GeTe_2 ($\sim 0.3\,\mu V\,K^{-1}$) [12], etc. Apart from the intrinsic mechanisms, extrinsic mechanisms such as asymmetric skew scattering can also give rise to large ANE coefficient especially in magnetic oxides, e.g., Fe_3O_4 single crystals [13], hole-doped manganite $La_{1-x}Na_xMnO_3$ [14], ferromagnetic cobaltites [15–17], etc.

Recently, spin gapless semiconductors (SGSs) have attracted immense attention of the spintronics community due to their unconventional electronic structures; while they exhibit a finite band gap for one spin channel, the conduction- and valence-band edges touch for the other spin channel [18]. Thus, they possess the characteristics of both half-metallic ferromagnets and gapless semiconductors. Because of such unique feature of their band structure, their transport properties are extremely susceptible to external stimuli, e.g., temperature and magnetic field which in combination with their high spin polarization make them potential tunable spintronic materials. Although the SGS behavior was originally predicted in diluted magnetic semiconductors (DMS), Heusler alloy-based SGS materials appear to be more advantageous than the DMS-based SGSs because of their high Curie temperature (T_C) and sizable spin polarization [19–22]. In addition to the well-studied topological Heusler alloy Co_2MnGa, the ANE has been extensively investigated in plenty of full-Heusler compounds, e.g., Co_2TiSn [23], $Ni_{46.5}Co_2Mn_{37}Sn_{14.5}$ [24], $Co_2Fe_{0.4}Mn_{0.6}Si$ [25], Co_2MnSi [26], $Co_2MnAl_{1-x}Si_x$ [27], Ni_2MnGa [28], etc. However, to our knowledge, ANE in Heusler alloy-based SGS materials has not been explored so far.

The quaternary Heusler alloys $Co_{1+x}Fe_{1-x}CrGa$ with very high Curie temperature ($T_C \geqslant 690$ K) were found to exhibit extraordinary SGS behavior for $x \leqslant 0.4$ but become completely half metallic for $x = 0.5$ [22,29]. Here, we have performed a comprehensive investigation of ANE in $Co_{1+x}Fe_{1-x}CrGa$ as a function of magnetic field and temper-

*Present address: Indian Institute of Technology Delhi, New Delhi–110016, India.

†suresh@phy.iitb.ac.in

‡phanm@usf.edu

§sharihar@usf.edu

ature. We found that the electron-electron elastic scattering and the weak localization effect play the dominant roles in electrical transport for all the samples at low temperatures, and the contributions from these scatterings increase considerably with x for $x \leqslant 0.4$. On the other hand, the magnon-drag effect was found to dominate the longitudinal thermoelectric transport in all the samples. Our study indicates that the ANE coefficient increases gradually with x for $x \leqslant 0.4$ but has a drastic increase for $x = 0.5$, when the system transforms from the SGS state to the completely half-metallic state. An in-depth analysis of the temperature dependence of transverse thermoelectric coefficient (S_{xy}), longitudinal Seebeck coefficient (S_{xx},) and the longitudinal resistivity (ρ_{xx}) indicates that the observed ANE in these samples originates from the skew-scattering mechanism.

II. EXPERIMENT

Polycrystalline samples of $Co_{1+x}Fe_{1-x}CrGa$ were synthesized by arc-melting technique. The synthesis method and the crystal-phase characterization of these samples are reported elsewhere [22,29]. The crystal structure of these samples was determined by x-ray-diffraction (XRD) pattern at room temperature using an Xpert pro diffractometer with Cu−Kα radiation ($\lambda = 1.541\,84$ Å). Static magnetic characterization of the samples was performed using a vibrating sample magnetometer attached to a commercial physical property measurement system (PPMS) from Quantum Design. Electrical resistivity (ρ_{xx}) measurements on these samples were performed using the DC resistivity option of the PPMS. Longitudinal thermopower (S_{xx}) measurements on these samples were carried out using a home-made sample stage for the PPMS. ANE on these samples were measured as a function of temperature and magnetic field using a custom-built spincaloritronic measurement setup by making use of a universal sample puck for the PPMS. The samples were sandwiched between two copper blocks (hot and cold). The bottom (hot) block was thermally detached from the PPMS puck base by a 4-mm-thick Teflon block to retain a temperature difference of ∼10 K between the PPMS puck base and the hot block. On the other hand, the top (cold) block was thermally connected to the PPMS puck base by a pair of molybdenum screws. To maintain a stable temperature difference between these two blocks, temperatures of both these blocks were controlled using PID (Proportional, Integral, Derivative) temperature controllers (Scientific Instruments 9700). Temperature gradient was applied between these two blocks using two Pt100 RTD sensors (used as resistive heaters) attached to both these blocks. A calibrated Si-diode thermometer was attached to each of these blocks that accurately recorded the temperatures $T_{\rm hot}$ and $T_{\rm cold}$ corresponding to temperatures of the hot and cold blocks, respectively. The sample temperature was recorded as the average temperature, $T_{\rm sample} = \frac{T_{\rm hot}+T_{\rm cold}}{2}$. In order to electrically insulate the sample surfaces from the copper blocks, a thin layer of kapton tape was thermally anchored to the bare surfaces of both the copper blocks. Note that the kapton tape acts as a good thermal conductor and poor electrical conductor. Additionally, cryogenic Apiezon N-grease was applied to the kapton tapes attached to the surfaces of both these blocks to ensure good thermal connectivity

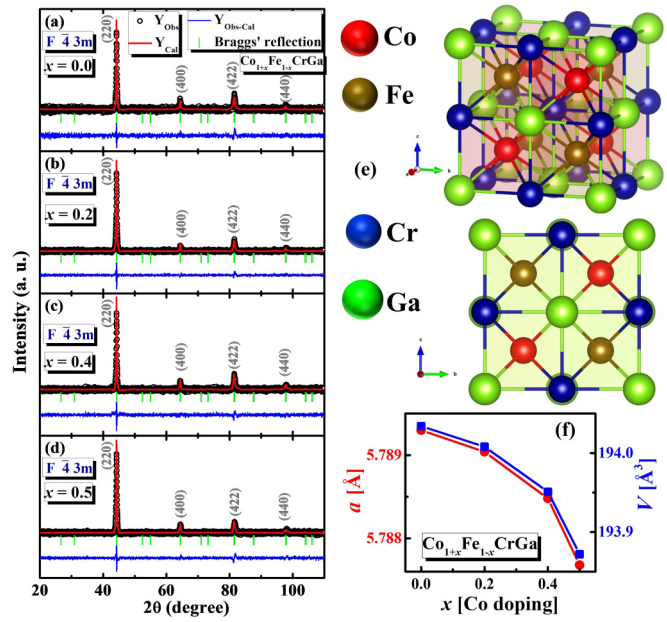

FIG. 1. XRD patterns for the samples: (a) $x = 0.0$, (b) $x = 0.2$, (c) $x = 0.4$, and (d) $x = 0.5$, respectively, in $Co_{1+x}Fe_{1-x}CrGa$ along with the Rietveld analysis. (e) Schematic illustration of the crystal structure of CoFeCrGa. (f) Variation of lattice parameter (left y scale) and unit-cell volume (right y scale) with x.

between the sample surfaces and the copper blocks. Moreover, both the temperature sensors were attached to the closest proximity of the sample surface in order to accurately read the temperatures of the hot and cold ends of the sample. A more detailed description of our experimental setup is reported elsewhere [30,31]. Note that the applied temperature difference between the hot and cold plates is primarily dropped across the sample and the influence of interfacial thermal resistances can be neglected, as discussed in the Supplemental Material [32–35]. The transverse thermoelectric voltage generated due to the ANE was measured using a Keithley 2182A nanovoltmeter, while scanning a DC magnetic field produced by the superconducting magnet of the PPMS. We used the same setup for temperature dependence of longitudinal Seebeck coefficient measurement. During the measurement at any specific temperature, a temperature gradient was applied between the hot and cold plates once the desired sample temperature was reached. Once a stable temperature difference between the hot and cold plates, ΔT was attained, the thermally generated voltage across the sample along the direction of the temperature gradient was recorded. The background voltage and other spurious contributions were eliminated by reversing the direction of the temperature gradient and averaging the thermally generated voltages.

III. RESULTS AND DISCUSSION

Figures 1(a)–1(d) demonstrate the room temperature XRD patterns for the samples $x = 0.0$, 0.2, 0.4, and 0.5, respectively, along with the Rietveld analysis performed using the FULLPROF SUITE software. The observed Bragg reflections indicate that these alloys adopt cubic crystal structure with space

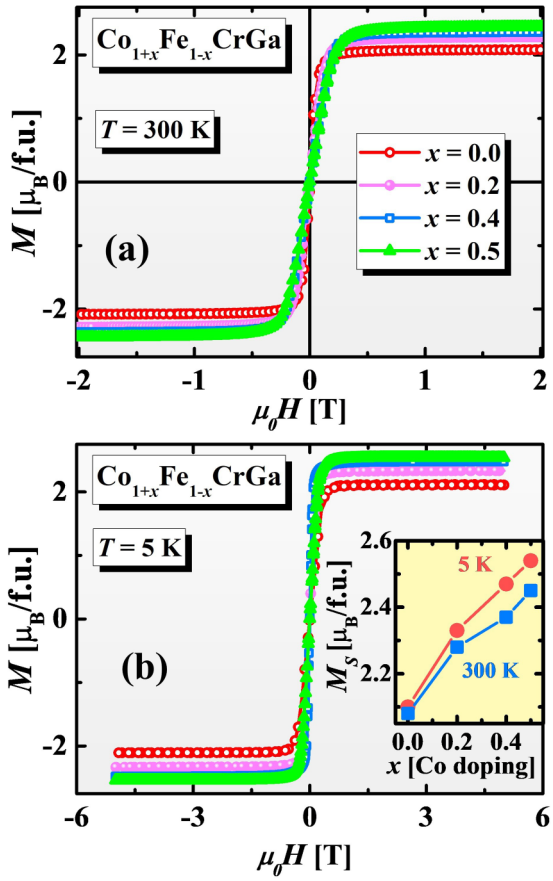

FIG. 2. Magnetic field dependence of magnetization, $M(H)$ for $Co_{1+x}Fe_{1-x}CrGa$ at (a) $T = 300$ K and (b) 5 K; inset of (b) shows x dependence of saturation magnetization, M_S.

group $F\bar{4}3m$ having the structural prototype of LiMgPdSn. Using synchrotron-based XRD measurements, our previous report [29] indicated the existence of the low-angle superlattices reflections (111) and (200) peaks, which are not visible in the standard XRD patterns, and hence, partially rules out the possibility of the presence of $B2$- and $A2$-type antisite disorders. On the other hand, an earlier report on Mössbauer spectroscopy performed on the pristine CoFeCrGa alloy confirmed the presence of DO_3-type disorder [22]. We believe that a certain amount of DO_3-type antisite disorder is present in all our samples [29].

A schematic representation of the crystal structure of CoFeCrGa is shown in Fig. 1(e), where Ga, Cr, Fe, and Co atoms occupy the Wyckoff positions of 4a, 4b, 4c, and 4d considering type I structure [36]. The lattice parameter (a) and unit-cell volume (V) were evaluated from the Rietveld analysis. As shown in Fig. 1(f), both a and V decrease gradually with increasing Co content, which is in agreement with the previous study [29].

Figures 2(a) and 2(b) display the magnetic field dependence of magnetization, $M(H)$, measured at $T = 300$ and 5 K on the Heusler alloy series $Co_{1+x}Fe_{1-x}CrGa$ with $x =$ 0.0, 0.2, 0.4, and 0.5. $M(H)$ for all the samples exhibit negligible hysteresis at both the temperatures, indicating the soft-magnetic nature of the samples. Most importantly, the saturation magnetization, M_S, of the samples increases monotonically with x at both the temperatures as shown in the inset of Fig. 2(b). The experimental values of M_S at $T = 5$ K for $x = 0$, 0.2, 0.4, and 0.5 are 2.1, 2.33, 2.47, and 2.54 μ_B/f.u., respectively, which are close to those estimated using the Slater-Pauling rule [37]. An earlier report shows that the magnetic transition temperature (T_C) of these samples is very high and it increases linearly from 686 K for $x = 0$ to 870 K for $x =$ 0.5 [29]. Figures 3(a) and 3(b) represent the T dependence of longitudinal resistivity, $\rho_{xx}(T)$, for the samples $x = 0$ and 0.5. While $\rho_{xx}(T)$ for $x = 0$ exhibits semiconducting behavior ($\frac{\partial \rho_{xx}}{\partial T} < 0$) throughout the measured temperature range, that for $x = 0.5$ shows metallic-like resistivity ($\frac{\partial \rho_{xx}}{\partial T} > 0$) from room temperature down to 50 K, at which it shows a minimum in ρ_{xx} followed by a remarkable upturn below $T^* \approx 50$ K [29]. A closer inspection reveals that $\rho_{xx}(T)$ for $x = 0$ also shows a weak slope change around $T^* = 50$ K (indicated by an arrow) below which ρ_{xx} increases at a faster rate with decreasing temperature. Note that $\rho_{xx}(T)$ for samples $x =$ 0.2 and 0.4 also exhibit semiconducting behavior throughout the measured temperature range with more pronounced slope changes at $T^* \approx 50$ K in comparison to $x = 0$ followed by enhanced $|\frac{\partial \rho_{xx}}{\partial T}|$ below $T^* \approx 50$ K. The relative change in ρ_{xx} below $T^* \approx 50$ K, $\frac{\Delta \rho_{xx}}{\rho_{xx}} = \frac{\rho_{xx}(T=10\text{ K}) - \rho_{xx}(T=50\text{ K})}{\rho_{xx}(T=50\text{ K})}$, increases from $\approx$0.05 for $x = 0$ to $\approx$0.1 for $x = 0.4$.

We start with the analysis of the $\rho_{xx}(T)$ data taking into consideration different bulk-scattering mechanisms. Generally, the electrical resistivity of a conducting material can be expressed as $\rho_{xx} = \rho_{xx}^{\text{elastic}} + \rho_{xx}^{\text{inelastic}}$ [38]. Here, $\rho_{xx}^{\text{elastic}}$ represents the contribution from electron-electron elastic scattering due to the Coulomb interaction between conduction electrons, which usually has a $T^{1/2}$ (i.e., $\rho_{xx}^{\text{elastic}} = \rho_e T^{1/2}$) and dominates at low T [39]. It is believed that the resistivity minimum accompanied by a low-T upturn can arise from elastic electron-electron interaction when the low-temperature resistivity exceeds the Mott maximum limit of metallic resistivity of $\approx$10 mΩ cm [38,39], which is much higher than the low-T value of ρ_{xx} (≈ 0.32 mΩ cm at 10 K for $x = 0$) for our samples. However, in a highly disordered 3D metal such as our $Co_{1+x}Fe_{1-x}CrGa$ system [29], the weak localization effect (WLE) [39] arising from the disorder-mediated coherent backscattering of charge carriers can also give rise to the low-T upturn in resistivity and it has the T dependence of $\sim T^{-1/2}$ [39–41]. On the other hand, the Kondo-like [42] transport arising from the interaction between localized magnetic moments associated with magnetic impurities and the mobile electrons can also give rise to the low-T upturn in resistivity in a disordered magnetic material and it has the T dependence of $\sim \ln T$ [39,43,44]. As shown in Fig. S1 [32], we fitted the $\rho_{xx}(T)$ data with the WLE and Kondo effect separately in the low-T region and found that the WLE can describe the upturn more effectively. Therefore, the rapid upturn in $\rho_{xx}(T)$ for $x = 0.5$ as well as the low-T slope change followed by enhanced $|\frac{\partial \rho_{xx}}{\partial T}|$ for $x =$ 0–0.4 below T^* possibly originate from the WLE [29]. On the other hand, $\rho_{xx}^{\text{inelastic}}$ signifies the contributions from different inelastic scattering mechanisms, such as electron-electron (ρ_{el-el}), electron-phonon (ρ_{el-ph}), electron-magnon (ρ_{el-mag}), and double-magnon (ρ_{mag}) scatterings in magnetic conductors [35]. Here, the electron-electron scattering contribution arises

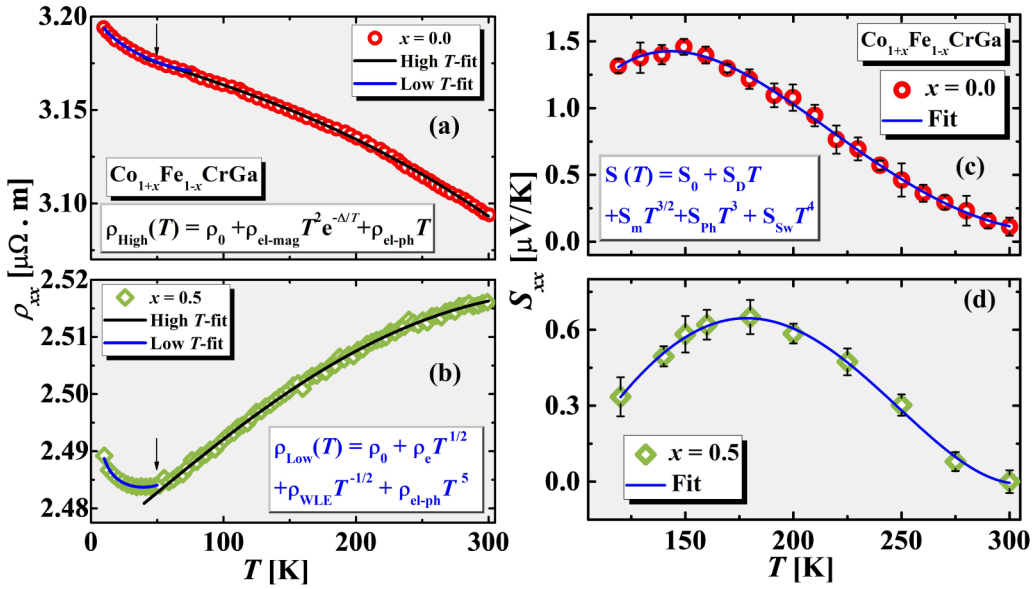

FIG. 3. Temperature dependence of longitudinal resistivity, $\rho_{xx}(T)$ for (a) $x = 0.0$ and (b) $x = 0.5$ in $Co_{1+x}Fe_{1-x}CrGa$, fitted with $\rho_{xx}(T) = \rho_0^{'} + \rho_{el-mag}T^2\ e^{-(\Delta/T)} + \rho_{el-ph}T$ in the high-temperature region and with $\rho_{xx}(T) = \rho_0 + \rho_e T^{1/2} + \rho_{WLE}T^{-1/2} + \rho_{el-ph}T^5$ in the low-temperature region. Temperature dependence of longitudinal Seebeck coefficient, $S_{xx}(T)$ for (c) $x = 0.0$ and (d) $x = 0.5$ fitted with $S_{xx}(T) = S_0 + S_d T + S_{mag}T^{3/2} + S_{ph}T^3 + S_{SW}T^4$.

due to inelastic collision between light (s electrons) and heavy electrons (d electrons) and usually varies as T^2 [45,46]. The contribution from the scattering of conduction electrons by lattice phonons follows T^5 behavior [44,47] at low T, but shows a T-linear behavior at high T [48]. The contribution of electron-magnon scattering towards resistivity also follows T^2 dependence [47]. However, in case of half metals [49,50], the T^2-dependent electron-magnon scattering contribution exponentially decays due to the gapped spin-flip scattering, and the contribution from electron-magnon scattering becomes, [50,51] $\rho_{e-m}(T) \propto T^2\ e^{-(\Delta/T)}$, where $k_B\Delta$ is the spin-wave energy gap which accounts for the difference between the Fermi level and the nearest band edge of unoccupied minority spins [50], and k_B is the Boltzmann constant. Nevertheless, there is an energy gap between the filled conduction and unoccupied valence-band edges associated with the minority spin channel for both half metals and spin gapless semiconductors [19,29]. Therefore, the aforementioned electron-magnon scattering model is valid for both the systems. It is also noteworthy that the contribution of the electron-electron inelastic scattering is insignificant compared to the other contributions [47]. Therefore, we have neglected the contribution of the electron-electron inelastic scattering towards $\rho_{xx}(T)$ for our $Co_{1+x}Fe_{1-x}CrGa$ system. We found that the $\rho_{xx}(T)$ data for all our samples were found to fit well with the expression: $\rho_{xx}(T) = \rho_0 + \rho_e T^{1/2} + \rho_{WLE}T^{-1/2} + \rho_{el-ph}T^5$ in the low-T (below the upturn) region and with the expression $\rho_{xx}(T) = \rho_0^{'} + \rho_{el-mag}T^2\ e^{-(\Delta/T)} + \rho_{el-ph}T$ in the high-T (above the upturn) region. Notably, for the low-temperature region, we excluded the electron-magnon scattering term as the electron-electron elastic scattering and weak localization are the most significant and dominating mechanisms for the resistivity upturn at low temperatures. Here, ρ_0 and $\rho_0^{'}$ are the residual resistivity arising from the scattering of conduction electrons by lattice defects and impurities, respectively [38,52].

The variations of the fitting parameters with Co doping are depicted in Fig. S3 [32]. For the high-temperature fits, the absolute values of ρ_{el-mag} and Δ increase with x for $x \leqslant 0.4$, but decrease considerably for $x = 0.5$. It is also evident that both ρ_{el-ph} and ρ_{el-mag} are negative for $x \leqslant 0.4$, which is expected as ρ_{xx} for these samples decreases with increasing temperature. However, the absolute value of ρ_{el-ph} does not vary significantly with x for $x \leqslant 0.4$, but changes its sign for $x = 0.5$, for which $\rho_{xx}(T)$ shows metallic-like behavior above the upturn. The obtained values of Δ for our $Co_{1+x}Fe_{1-x}CrGa$ system are higher than those reported for the well-known half-metallic CrO_2 ($\Delta \approx 80$ K) [51], Fe_2Si ($\Delta \approx 85$ K) [49], and Co_2FeSi ($\Delta \approx 100$ K) [50], etc. However, the value of Δ is lower in the sample $x = 0.5$ (half metal) compared to the samples $x \leqslant 0.4$ (spin gapless semiconductors) in our $Co_{1+x}Fe_{1-x}CrGa$ system. On the other hand, it is apparent that the absolute values of ρ_e and ρ_{WLE} in the low-temperature region increase with x for $x \leqslant 0.4$, but decrease for $x = 0.5$. Clearly, ρ_e is negative for all the samples which is expected at low temperatures. Negative temperature coefficient for the electron-electron scattering is reported in different Heusler alloys [41,53] as well as disordered manganites [52] showing low-temperature resistivity upturns. However, ρ_{el-ph} decreases slightly with x for $x \leqslant 0.4$ but increases for $x = 0.5$. Nevertheless, the absolute value of ρ_{el-ph} is extremely small compared to that of ρ_e and ρ_{WLE} for all the samples, indicating that the electron-electron elastic scattering and WLE play the dominant roles in electrical transport for all the samples at low temperatures.

Next, we focus on the thermoelectric transport in our $Co_{1+x}Fe_{1-x}CrGa$ system. Figures 3(c) and 3(d) represent the T dependence of longitudinal thermopower, $S_{xx}(T)$, for the

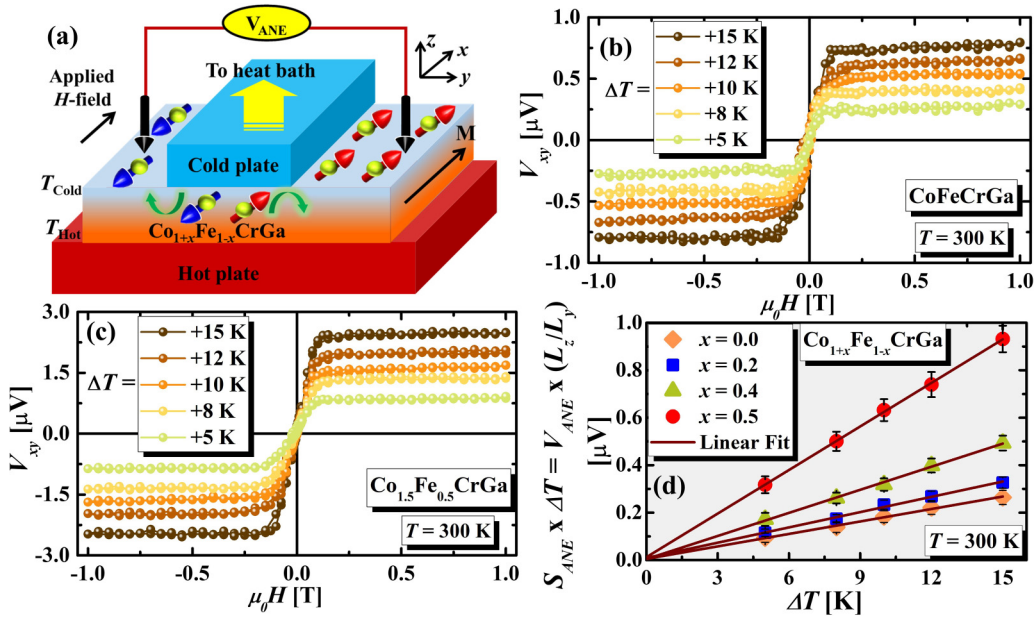

FIG. 4. (a) Schematic illustration of ANE measurement on the $Co_{1+x}Fe_{1-x}CrGa$ samples. Magnetic field dependence of the Nernst voltage, $V_{xy}(H)$ for different values of ΔT for (b) $x = 0.0$ and (c) $x = 0.5$ at $T = 300$ K. (d) Normalized anomalous Nernst voltage, $S_{\rm ANE} \times \Delta T = V_{\rm ANE}(\mu_0 H_{\rm sat}) \times (\frac{L_z}{L_y})$, as a function of ΔT showing linear ΔT dependence.

samples $x = 0.0$ and 0.5. The sign of $S_{xx}(T)$ for all the samples is positive, indicating holes as the dominant carrier for the thermally driven charge transport. For a 3D semiconductor, the diffusive component of the longitudinal thermopower follows the relation $S_{xx}^{3D}(T) = m_d^* \frac{8\pi^2 k_B^2 T}{3eh^2}(\frac{\pi}{N})^{2/3}$, where $N =$ carrier concentration, $m_d^* =$ effective mass, $k_B =$ Boltzmann constant, $e =$ electronic charge, and $h =$ Planck's constant [54]. We noticed that the value of S_{xx} increases with x for $x \leqslant 0.4$ but then decreases for $x = 0.5$. Most importantly, for all the samples, $S_{xx}(T)$ shows a broad maximum which shifts from $T_P \sim 150$ K for $x = 0$ to ~ 175 K for $x = 0.5$. Note that the peak in thermopower at low temperatures can arise due to the phonon-drag or magnon-drag effects [55,56]. In a ferromagnetic conductor, electrons are scattered by spin waves, and this electron-magnon interaction is responsible for magnon-drag effect, which is very similar to phonon-drag effect caused by electron-phonon scattering. While the contribution of phonon-drag effect in thermopower shows T^3 dependence [55,56], the magnon-drag effect is closely related to the magnon specific heat and hence, it has the T dependence of $T^{3/2}$ [55,57]. Therefore, we fitted our $S_{xx}(T)$ data for all the samples using the expression $S_{xx}(T) = S_0 + S_d T + S_{\rm mag} T^{3/2} + S_{\rm ph} T^3 + S_{\rm SW} T^4$, where, the second, third, fourth, and fifth terms account for contributions from diffusion, magnon-drag effect, phonon-drag effect, and spin-wave fluctuations, respectively [57,58]. The variations of the fitting parameters with Co doping are shown in Fig. S5 [32]. It is evident that the absolute value of $S_{\rm mag}$ is ~ 4 orders of magnitude higher than that of $S_{\rm ph}$, indicating dominant contribution of the magnon-drag effect. Note that the phonon-drag effect-induced maximum in $S_{xx}(T)$ generally occurs around $T \approx (\theta_D/5)$ [56], where θ_D is the Debye temperature. Since θ_D was found to be ≈ 425 K for $Co_{1.1}Fe_{0.9}GaCr$ [29], the phonon-drag driven maximum in $S_{xx}(T)$ is expected to occur ≈ 85 K. Since the broad maxima in $S_{xx}(T)$ occur at or above 150 K for all our samples, the magnon-drag effect is certainly the dominating mechanism for the broad peak and hence, for the thermoelectric transport in our $Co_{1+x}Fe_{1-x}CrGa$ system.

Anomalous Nernst effect measurements on the $Co_{1+x}Fe_{1-x}CrGa$ samples were performed by sandwiching the samples between two copper blocks kept at different temperatures, as shown in Fig. 4(a). A photograph of the actual setup along with the measurement schematic is presented in Fig. S6 [32]. A temperature gradient was applied along the z direction that generates a vertical temperature difference, $\Delta T = (T_{\rm hot} - T_{\rm cold})$, between the bottom (hot) and top (cold) blocks that generates a transverse Nernst voltage along the y direction. In Figs. 4(b) and 4(c), we show the magnetic field dependence of the Nernst voltage, $V_{xy}(H)$, for different values of ΔT for $x = 0.0$ and 0.5 in $Co_{1+x}Fe_{1-x}CrGa$, respectively, at a fixed temperature $T = \frac{T_{\rm hot}+T_{\rm cold}}{2} = 300$ K. The isothermal $V_{xy}(H)$ loops show negligible hysteresis for all the samples, replicating their $M(H)$ behavior. It is clearly seen that the $V_{xy}(H)$ signal strength increases with increasing the value of ΔT.

In Fig. 4(d), we present normalized anomalous Nernst voltage, $S_{\rm ANE} \times \Delta T = V_{\rm ANE}(\mu_0 H_{\rm sat}) \times (\frac{L_z}{L_y})$, as a function of ΔT for the samples $Co_{1+x}Fe_{1-x}CrGa$ at $T = 300$ K, where $V_{\rm ANE}(\mu_0 H_{\rm sat})$ is the background-corrected anomalous Nernst voltage defined as $V_{\rm ANE}(\mu_0 H_{\rm sat}) = [\frac{V_{xy}(+\mu_0 H_{\rm sat}) - V_{xy}(-\mu_0 H_{\rm sat})}{2}]$, where $\mu_0 H_{\rm sat}$ is the saturation field, $S_{\rm ANE}$ is the anomalous Nernst coefficient, L_y (= 3 mm for all the samples) is the separation between the voltage leads, and L_z is the sample thickness along which the ΔT was applied. It is evident that $(S_{\rm ANE} \times \Delta T)$ varies linearly with ΔT for all the samples, indicating intrinsic contribution of the thermally induced ANE signal [13,15].

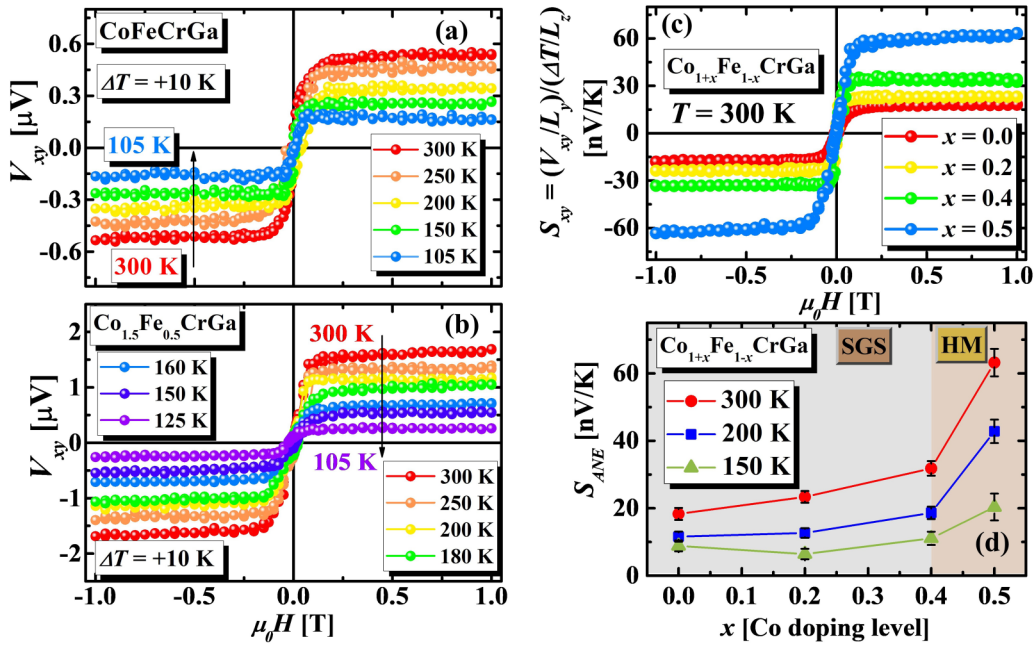

FIG. 5. $V_{xy}(H)$ Hysteresis loops for (a) $x = 0.0$ and (b) $x = 0.5$ in $Co_{1+x}Fe_{1-x}CrGa$ at few selected temperatures for $\Delta T = +10$ K. (c) Comparison of the magnetic field dependence of the transverse Seebeck coefficient, $S_{xy}(H) = \frac{V_{xy}(H)}{\Delta T} \times (\frac{L_z}{L_y})$, for all the samples in the series $Co_{1+x}Fe_{1-x}CrGa$ at $T = 300$ K for $\Delta T = +10$ K. (d) Comparison of the x dependence of the background-corrected anomalous Nernst coefficient, $S_{\rm ANE}(\mu_0 H_{\rm sat}) = \frac{V_{\rm ANE}(\mu_0 H_{\rm sat})}{\Delta T} \times (\frac{L_z}{L_y}) = \frac{1}{2}\frac{[V_{xy}(+\mu_0 H_{\rm sat}) - V_{xy}(-\mu_0 H_{\rm sat})]}{\Delta T} \times (\frac{L_z}{L_y})$, at $T = 300$, 200, and 150 K.

Figures 5(a) and 5(b) demonstrate the $V_{xy}(H)$ hysteresis loops for the samples $x = 0$ and 0.5 in $Co_{1+x}Fe_{1-x}CrGa$, respectively, at few selected temperatures for a fixed value of $\Delta T = +10$ K. The $V_{xy}(H)$ hysteresis loops at different temperatures for the samples $x = 0.2$ and 0.4 are shown in Fig. S8 [32]. It is evident that the $V_{xy}(H)$ signal strength decreases with reducing temperature. In Fig. 5(c), we compare the magnetic field dependence of the transverse Seebeck coefficient, $S_{xy}(H)$, defined as $S_{xy}(H) = \frac{V_{xy}(H)}{\Delta T} \times (\frac{L_z}{L_y})$ for all the samples in the series $Co_{1+x}Fe_{1-x}CrGa$ at $T = 300$ K for $\Delta T = +10$ K. Clearly, the $S_{xy}(H)$ signal increases with increasing Co doping (x). This is consistent with the fact that the thermally generated electric field induced by ANE is proportional to the magnetization through the expression [4,13] $\overrightarrow{E_{ANE}} \propto (\mu_0 \vec{M} \times \vec{\nabla T})$, and M_S of the samples $Co_{1+x}Fe_{1-x}CrGa$ also increases with x. In this context, let us consider the contribution of the ordinary Nernst effect (NE) which is linearly proportional to the applied magnetic field, $\overrightarrow{E_{NE}} \propto (\vec{H} \times \vec{\nabla T})$. The ordinary Nernst contribution, S_{NE}, was estimated from the slope of the slowly varying segment of the $S_{xy}(H)$ vs H curves (i.e., for $H \geqslant H_{\rm sat}$) [13,15]. We found that $|S_{NE}| \approx 1.17 \times 10^{-4}$, 1.15×10^{-4}, 5.2×10^{-5}, and 7.6×10^{-4} nV K^{-1}, for $x = 0$, 0.2, 0.4, and 0.5, respectively, at $T = 300$ K. Therefore, the ordinary NE contributes only ≈0.001% of the total Nernst signal and hence can be neglected, which indicates the dominant contribution of ANE in these samples. Figure 5(d) compares the Co doping level (x) dependence of the background-corrected anomalous Nernst coefficient, $S_{\rm ANE}(\mu_0 H_{\rm sat}) = \frac{V_{\rm ANE}(\mu_0 H_{\rm sat})}{\Delta T} \times (\frac{L_z}{L_y}) = \frac{1}{2}\frac{[V_{xy}(+\mu_0 H_{\rm sat}) - V_{xy}(-\mu_0 H_{\rm sat})]}{\Delta T} \times (\frac{L_z}{L_y})$ at $T = 300$, 200, and 150 K. It is evident that $S_{\rm ANE}(\mu_0 H_{\rm sat})$ increases slowly with x for $x \leqslant$ 0.4 but rapidly between $x = 0.4$ and 0.5 (when it transforms from SGS state to completely half-metallic state), whereas M_S increases linearly with x, which signifies that the ANE signal is not solely governed by the magnetization of the samples. The value of $S_{\rm ANE}$ for $x = 0.5$ at $T = 300$ K is 0.063 μV K^{-1}, which is higher than that for $Ni_{81}Fe_{19}$ (0.048 μV K^{-1}) [59] and compressively strained $SrRuO_3$ films (0.03 μV K^{-1}) [60].

We show the temperature dependence of the anomalous Nernst coefficient $S_{\rm ANE}(T)$ for the samples $x = 0$, 0.2, 0.4, and 0.5 in Figs. 6(a), 6(b), 6(c), and 6(d), respectively. Notably, $S_{\rm ANE}(T)$ for $x = 0$ decreases almost linearly with T in the temperature range 105 K $\leqslant T \leqslant$ 300 K. However, for the samples $x = 0.2$ and 0.4, we could get good ANE signal only up to 150 K, and observed nearly T-linear behavior in $S_{\rm ANE}(T)$ for these two samples. Most interestingly, $S_{\rm ANE}(T)$ for the sample $x = 0.5$ shows T-linear behavior in the range 200 K $\leqslant T \leqslant$ 300 K, but undergoes a prominent slope change at 200 K followed by a nonlinear T dependence which is accompanied by a rapid decrease down to 125 K. In order to understand the underlying mechanism for the observed behavior of $S_{\rm ANE}(T)$ in the series $Co_{1+x}Fe_{1-x}CrGa$, let us begin with the correlations among S_{xy}, S_{xx}, ρ_{xx}, and the transverse thermoelectric conductivity (the Nernst conductivity) α_{xy}, which can be expressed as $S_{xy} = \rho_{xx}(\alpha_{xy} - S_{xx}\sigma_{xy})$, where σ_{xy} is the transverse electrical conductivity [13]. While S_{xx} is related to the energy derivative of the longitudinal electrical conductivity σ_{xx} at the Fermi level E_F through the expression [3,61] $S_{xx} = \frac{\pi^2 k_B^2 T}{3e\sigma_{xx}}(\frac{\partial \sigma_{xx}}{\partial E})_{E=E_F}$, α_{xy} is connected to the energy derivative of σ_{xy} at E_F through the Mott relation [3], $\alpha_{xy} = \frac{\pi^2 k_B^2 T}{3e}(\frac{\partial \sigma_{xy}}{\partial E})_{E=E_F}$. Let us recall the power law for the anomalous Hall effect, which connects the transverse (ρ_{xy}) and the longitudinal resistivity (ρ_{xx}) through the relation $\rho_{xy} =$

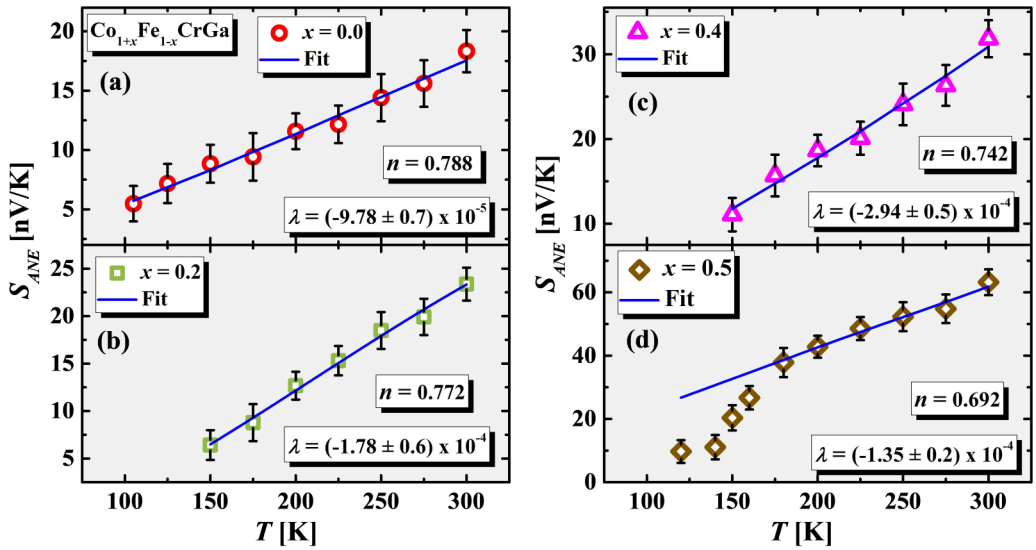

FIG. 6. Temperature dependence of the anomalous Nernst coefficient, $S_{\mathrm{ANE}}(T)$, for (a) $x = 0.0$, (b) $x = 0.2$, (c) $x = 0.4$, and (d) $x = 0.5$ fitted with Eq. (1).

$\lambda\rho_{xx}^{n}$, where λ is the spin-orbit coupling constant. Considering all the above-mentioned relations, S_{xy} can be expressed as [3,13]

$$S_{xy} = \rho_{xx}^{n-1}\left[\frac{\pi^2 k_B^2 T}{3e}\left(\frac{\partial\lambda}{\partial E}\right)_{E=E_F} - (n-1)\lambda S_{xx}\right]. \quad (1)$$

Note that when $n = 1$, skew scattering is the dominating mechanism for the anomalous Nernst transport and S_{xy} will be independent/weakly dependent on the bulk electrical transport as well as longitudinal thermoelectric properties of the material [62]. On the contrary, when $n = 2$, the intrinsic Berry curvature, or the side jump, is the dominating mechanism for the anomalous Nernst transport [62]. Incorporating the $\rho_{xx}(T)$ and $S_{xx}(T)$ data, we fitted the $S_{\mathrm{ANE}}(T)$ data for our $Co_{1+x}Fe_{1-x}CrGa$ samples using Eq. (1) taking λ, $(\frac{\partial\lambda}{\partial E})_{E=E_F}$, and n as the fitting parameter. We found that $S_{\mathrm{ANE}}(T)$ for samples $x = 0$–0.4 fits well with Eq. (1) throughout the measured temperature range, whereas that for $x = 0.5$ fits well only for $200\ \mathrm{K} \leqslant T \leqslant 300\ \mathrm{K}$ and deviates below 200 K. The value of n was found to decrease from 0.788 for $x = 0$ to 0.692 for $x = 0.5$ which signifies that the origin of ANE in the series $Co_{1+x}Fe_{1-x}CrGa$ is dominated by skew-scattering mechanism [13–15,62].

We found that $|\lambda|$ increases from $(9.78 \pm 0.7) \times 10^{-5}$ for $x = 0$ to $(2.94 \pm 0.5) \times 10^{-4}$ for $x = 0.4$ but then decreases to $(1.35\ 0.6) \times 10^{-4}$ for $x = 0.5$. Moreover, the estimated values of $(\frac{\partial\lambda}{\partial E})_{E=E_F}$ for the samples $x = 0$, 0.2, 0.4, and 0.5 are $(1.02 \pm 0.02) \times 10^{15}$, $(1.11 \pm 0.05) \times 10^{15}$, $(1.17 \pm 0.04) \times 10^{15}$, and $(9.87 \pm 0.16) \times 10^{14}$, respectively. Note that the absolute values of both $|\lambda|$ and $(\frac{\partial\lambda}{\partial E})_{E=E_F}$ are quite close to those obtained for Fe_3O_4 single crystals [13]. It is known that the Hall angle is related to λ and ρ_{xx} through the expression $\tan\theta_{xy} = \frac{\sigma_{xy}}{\sigma_{xx}} = \frac{\lambda}{\rho_{xx}^{1-n}}$ [13]. Since $(1-n) > 0$ for our $Co_{1+x}Fe_{1-x}CrGa$ samples, $\lambda \propto \rho_{xx}^{1-n}$, and hence the x dependence of $|\lambda|$ should follow the behavior of x dependence of ρ_{xx}. Interestingly, as shown in Fig. 7, the x dependence

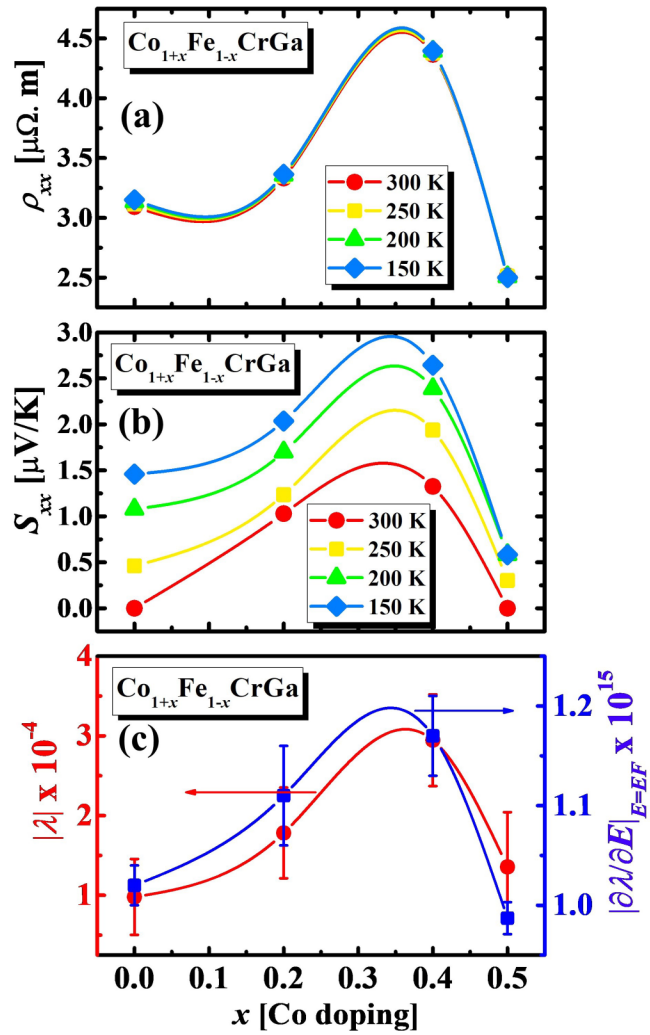

FIG. 7. The x dependence of (a) ρ_{xx} and (b) S_{xx} at $T = 300$, 250, 200, and 150 K in $Co_{1+x}Fe_{1-x}CrGa$. (c) The x dependence of $|\lambda|$ (left y axis) and $(\frac{\partial\lambda}{\partial E})_{E=E_F}$ (right y axis).

of both $|\lambda|$ and $(\frac{\partial\lambda}{\partial E})_{E=E_F}$ for $Co_{1+x}Fe_{1-x}CrGa$ follow the trend of x dependence of ρ_{xx} as well as S_{xx}, indicating the significant role of longitudinal electrical and thermoelectric transport properties in anomalous Nernst transport in this system. Our comprehensive studies reported in this paper emphasize that there are several possibilities to enhance the conversion efficiency of heat into Nernst thermopower by tuning the chemical composition of SGSs and therefore, they can be very promising candidates for extremely tunable highly efficient spin-caloritronics based device applications.

IV. CONCLUSIONS

In summary, we present a comprehensive investigation of the anomalous Nernst effect in the quaternary Heusler alloy-based spin gapless semiconductors $Co_{1+x}Fe_{1-x}CrGa$. We found that the electron-electron elastic scattering and the disorder-mediated weak localization effect play the major roles in electrical transport for all the samples at low temperatures, whereas the magnon-drag effect is found to dominate the longitudinal thermoelectric transport. The ANE coefficient, S_{ANE} increases slowly with x for $x \leqslant 0.4$ but rapidly between $x = 0.4$ and 0.5, when the system transforms from the SGS state to the completely half-metallic state. The value of S_{ANE} for $x = 0.5$ at $T = 300\,K$ is $0.063\,\mu V\,K^{-1}$, which is higher than that for $Ni_{81}Fe_{19}$ and compressively strained $SrRuO_3$ films. Our analysis indicates that the observed ANE originates from asymmetric skew scattering of charge carriers.

ACKNOWLEDGMENTS

Financial support by the US Department of Energy, Office of Basic Energy Sciences, Division of Materials Science and Engineering under Award No. DE-FG02-07ER46438. H.S. also thanks IIT Bombay for support from a short-term visiting professorship.

[1] G. E. W. Bauer, E. Saitoh, and B. J. Van Wees, Spin caloritronics, Nat. Mater. **11**, 391 (2012).

[2] M. Ikhlas, T. Tomita, T. Koretsune, M.-T. Suzuki, D. Nishio-Hamane, R. Arita, Y. Otani, and S. Nakatsuji, Large anomalous Nernst effect at room temperature in a chiral antiferromagnet, Nat. Phys. **13**, 1085 (2017).

[3] Y. Pu, D. Chiba, F. Matsukura, H. Ohno, and J. Shi, Mott Relation for Anomalous Hall and Nernst Effects in Ga 1- x Mn x As Ferromagnetic Semiconductors, Phys. Rev. Lett. **101**, 117208 (2008).

[4] A. Sakai, Y. P. Mizuta, A. A. Nugroho, R. Sihombing, T. Koretsune, M.-T. Suzuki, N. Takemori, R. Ishii, D. Nishio-Hamane, R. Arita *et al.*, Giant anomalous Nernst effect and quantum-critical scaling in a ferromagnetic semimetal, Nat. Phys. **14**, 1119 (2018).

[5] H. Yang, W. You, J. Wang, J. Huang, C. Xi, X. Xu, C. Cao, M. Tian, Z.-A. Xu, J. Dai *et al.*, Giant anomalous Nernst effect in the magnetic Weyl semimetal $Co_3Sn_2S_2$, Phys. Rev. Mater. **4**, 024202 (2020).

[6] L. Ding, J. Koo, L. Xu, X. Li, X. Lu, L. Zhao, Q. Wang, Q. Yin, H. Lei, B. Yan *et al.*, Intrinsic Anomalous Nernst Effect Amplified by Disorder in a Half-Metallic Semimetal, Phys. Rev. X **9**, 041061 (2019).

[7] A. Sakai, S. Minami, T. Koretsune, T. Chen, T. Higo, Y. Wang, T. Nomoto, M. Hirayama, S. Miwa, D. Nishio-Hamane *et al.*, Iron-based binary ferromagnets for transverse thermoelectric conversion, Nature (London) **581**, 53 (2020).

[8] T. Chen, S. Minami, A. Sakai, Y. Wang, Z. Feng, T. Nomoto, M. Hirayama, R. Ishii, T. Koretsune, R. Arita *et al.*, Large anomalous Nernst effect and nodal plane in an iron-based kagome ferromagnet, Sci. Adv. **8**, eabk1480 (2022).

[9] D. Khadka, T. R. Thapaliya, S. Hurtado Parra, J. Wen, R. Need, J. M. Kikkawa, and S. X. Huang, Anomalous Hall and Nernst effects in epitaxial films of topological kagome magnet Fe_3Sn_2, Phys. Rev. Mater. **4**, 084203 (2020).

[10] T. Asaba, V. Ivanov, S. M. Thomas, S. Y. Savrasov, J. D. Thompson, E. D. Bauer, and F. Ronning, Colossal anomalous Nernst effect in a correlated noncentrosymmetric kagome ferromagnet, Sci. Adv. **7**, eabf1467 (2021).

[11] Y. Pan, C. Le, B. He, S. J. Watzman, M. Yao, J. Gooth, J. P. Heremans, Y. Sun, and C. Felser, Giant anomalous Nernst signal in the antiferromagnet $YbMnBi_2$, Nat. Mater. **21**, 203 (2022).

[12] J. Xu, W. A. Phelan, and C.-L. Chien, Large anomalous Nernst effect in a van der Waals ferromagnet Fe_3GeTe_2, Nano Lett. **19**, 8250 (2019).

[13] R. Ramos, M. H. Aguirre, A. Anadón, J. Blasco, I. Lucas, K. Uchida, P. A. Algarabel, L. Morellón, E. Saitoh, and M. R. Ibarra, Anomalous Nernst effect of Fe_3O_4 single crystal, Phys. Rev. B **90**, 054422 (2014).

[14] A. Ghosh, R. Das, and R. Mahendiran, Skew scattering dominated anomalous Nernst effect in $La_{1-x}Na_xMnO_3$, J. Appl. Phys. **125**, 153902 (2019).

[15] A. Ghosh, A. Chanda, and R. Mahendiran, Anomalous Nernst effect in $Pr_{0.5}Sr_{0.5}CoO_3$, AIP Adv. **11**, 35031 (2021).

[16] A. Ghosh, A. Chanda, M. Manikandan, and R. Mahendiran, Rare earth size dependence of Nernst thermopower in ferromagnetic perovskites: $R_{0.6}Sr_{0.4}CoO_3$ (R = La, Pr, and Nd), J. Magn. Magn. Mater. **537**, 168240 (2021).

[17] T. Miyasato, N. Abe, T. Fujii, A. Asamitsu, S. Onoda, Y. Onose, N. Nagaosa, and Y. Tokura, Crossover Behavior of the Anomalous Hall Effect and Anomalous Nernst Effect in Itinerant Ferromagnets, Phys. Rev. Lett. **99**, 086602 (2007).

[18] X. L. Wang, Proposal for a New Class of Materials: Spin Gapless Semiconductors, Phys. Rev. Lett. **100**, 156404 (2008).

[19] S. Ouardi, G. H. Fecher, C. Felser, and J. Kübler, Realization of Spin Gapless Semiconductors: The Heusler Compound Mn_2CoAl, Phys. Rev. Lett. **110**, 100401 (2013).

[20] V. Alijani, J. Winterlik, G. H. Fecher, S. S. Naghavi, and C. Felser, Quaternary half-metallic Heusler ferromagnets for spintronics applications, Phys. Rev. B **83**, 184428 (2011).

[21] L. Bainsla, A. I. Mallick, M. M. Raja, A. K. Nigam, B. S. D. C. S. Varaprasad, Y. K. Takahashi, A. Alam, K. G. Suresh, and K. Hono, Spin gapless semiconducting behavior in equiatomic

quaternary CoFeMnSi Heusler alloy, Phys. Rev. B **91**, 104408 (2015).

[22] L. Bainsla, A. I. Mallick, M. M. Raja, A. A. Coelho, A. K. Nigam, D. D. Johnson, A. Alam, and K. G. Suresh, Origin of spin gapless semiconductor behavior in CoFeCrGa: Theory and experiment, Phys. Rev. B **92**, 045201 (2015).

[23] J. Hu, B. Ernst, S. Tu, M. Kuveždić, A. Hamzić, E. Tafra, M. Basletić, Y. Zhang, A. Markou, C. Felser, and Others, Anomalous Hall and Nernst Effects in Co_2TiSn and $Co_2Ti_{0.6}V_{0.4}Sn$ Heusler Thin Films, Phys. Rev. Appl. **10**, 044037 (2018).

[24] A. Ghosh, A. De, and S. Nair, Large anomalous Nernst effect across the magneto-structural transition in a bulk Ni-Co-Mn-Sn full Heusler alloy, Appl. Phys. Lett. **113**, 262405 (2018).

[25] J. Hu, T. Butler, M. A. Cabero Z., H. Wang, B. Wei, S. Tu, C. Guo, C. Wan, X. Han, S. Liu *et al.*, Regulating the anomalous Hall and Nernst effects in Heusler-based trilayers, Appl. Phys. Lett. **117**, 62405 (2020).

[26] C. D. W. Cox, A. J. Caruana, M. D. Cropper, and K. Morrison, Anomalous Nernst effect in Co_2MnSi thin films, J. Phys. D: Appl. Phys. **53**, 35005 (2019).

[27] Y. Sakuraba, K. Hyodo, A. Sakuma, and S. Mitani, Giant anomalous Nernst effect in the $Co_2MnAl_{1-x}Si_x$ Heusler alloy induced by Fermi level tuning and atomic ordering, Phys. Rev. B **101**, 134407 (2020).

[28] A. De, A. K. Singh, S. Singh, and S. Nair, Temperature dependence of the anomalous Nernst effect in Ni_2Mn Ga shape memory alloy, Phys. Rev. B **103**, L020404 (2021).

[29] D. Rani, Enamullah, L. Bainsla, K. G. Suresh, and A. Alam, Spin-gapless semiconducting nature of Co-rich Co_{1+x} Fe_{1-x} CrGa, Phys. Rev. B **99**, 104429 (2019).

[30] A. Chanda, C. Holzmann, N. Schulz, J. Seyd, M. Albrecht, M.-H. Phan, and H. Srikanth, Scaling of the thermally induced sign inversion of longitudinal spin Seebeck effect in a compensated ferrimagnet: Role of magnetic anisotropy, Adv. Funct. Mater. **32**, 2109170 (2022).

[31] A. Chanda, D. DeTellem, Y. T. Hai Pham, J. E. Shoup, A. T. Duong, R. Das, S. Cho, D. V. Voronine, M. T. Trinh, D. A. Arena *et al.*, Spin Seebeck effect in iron oxide thin films: Effects of phase transition, phase coexistence, and surface magnetism, ACS Appl. Mater. Interfaces **14**, 13468 (2022).

[32] See Supplemental Material at http://link.aps.org/supplemental/10.1103/PhysRevB.106.134416 for additional transport data.

[33] J. Nag, D. Rani, D. Singh, R. Venkatesh, B. Sahni, A. K. Yadav, S. N. Jha, D. Bhattacharyya, P. D. Babu, K. G. Suresh *et al.*, CoFeVSb: A promising candidate for spin valve and thermoelectric applications, Phys. Rev. B **105**, 144409 (2022).

[34] A. C. Anderson, R. B. Rauch, and M. M. Kreitman, Another comparison of thermal bonding agents, Rev. Sci. Instrum. **41**, 469 (1970).

[35] E. Gmelin, M. Asen-Palmer, M. Reuther, and R. Villar, Thermal boundary resistance of mechanical contacts between solids at sub-ambient temperatures, J. Phys. D: Appl. Phys. **32**, R19 (1999).

[36] B. Shi, J. Li, C. Jin, J. Yang, C. Zhang, Y. Yan, Y. Wang, and G. Zhang, Distinct transport behaviors and electronic structures in Heusler alloys CoFeCrGa and CoFeCrAl, J. Magn. Magn. Mater. **517**, 167383 (2021).

[37] I. Galanakis, P. H. Dederichs, and N. Papanikolaou, Slater-Pauling behavior and origin of the half-metallicity of the full-Heusler alloys, Phys. Rev. B **66**, 174429 (2002).

[38] D. S. Rana, J. H. Markna, R. N. Parmar, D. G. Kuberkar, P. Raychaudhuri, J. John, and S. K. Malik, Low-temperature transport anomaly in the magnetoresistive compound $(La_{0.5}Pr_{0.2})$ $Ba_{0.3}MnO_3$, Phys. Rev. B **71**, 212404 (2005).

[39] P. A. Lee and T. V. Ramakrishnan, Disordered electronic systems, Rev. Mod. Phys. **57**, 287 (1985).

[40] C. Cirillo, C. Barone, H. Bradshaw, F. Urban, A. Di Bernardo, C. Mauro, J. W. A. Robinson, S. Pagano, and C. Attanasio, Magnetotransport and magnetic properties of amorphous $(NdNi_5)$ thin films, Sci. Rep. **10**, 054410 (2020).

[41] D. Gnida, K. Ciesielski, and D. Kaczorowski, Origin of the negative temperature coefficient of resistivity in the half-Heusler antimonides LuNiSb and YPdSb, Phys. Rev. B **103**, 174206 (2021).

[42] J. Kondo, Resistance minimum in dilute magnetic alloys, Prog. Theor. Phys. **32**, 37 (1964).

[43] A. N. Pasupathy, R. C. Bialczak, J. Martinek, J. E. Grose, L. A. K. Donev, P. L. McEuen, and D. C. Ralph, The Kondo effect in the presence of ferromagnetism, Science **306**, 86 (2004).

[44] J. Zhang, Y. Xu, S. Cao, G. Cao, Y. Zhang, and C. Jing, Kondo-like transport and its correlation with the spin-glass phase in perovskite manganites, Phys. Rev. B **72**, 054410 (2005).

[45] K. Yamada, M. Nakano, K. Yoshida, K. Hanzawa, and A. Sakurai, T-square term of electrical resistivity, Prog. Theor. Phys. **82**, 689 (1989).

[46] A. Urushibara, Y. Moritomo, T. Arima, A. Asamitsu, G. Kido, and Y. Tokura, Insulator-metal transition and giant magnetoresistance in $La_{1-x}Sr_xMnO_3$, Phys. Rev. B **51**, 14103 (1995).

[47] S. Chatterjee, S. Chatterjee, S. Giri, and S. Majumdar, Transport properties of Heusler compounds and alloys, J. Phys.: Condens. Matter **34**, 013001 (2022).

[48] D. Kim, Q. Li, P. Syers, N. P. Butch, J. Paglione, S. Das Sarma, and M. S. Fuhrer, Intrinsic Electron-Phonon Resistivity of Bi_2Se_3 in the Topological Regime, Phys. Rev. Lett. **109**, 166801 (2012).

[49] A. W. Forbes, R. P. Dulal, N. Bhattarai, I. L. Pegg, and J. Philip, Experimental realization and magnetotransport properties of half-metallic Fe_2Si, J. Appl. Phys. **125**, 243902 (2019).

[50] D. Bombor, C. G. F. Blum, O. Volkonskiy, S. Rodan, S. Wurmehl, C. Hess, and B. Büchner, Half-Metallic Ferromagnetism with Unexpectedly Small Spin Splitting in the Heusler Compound Co_2FeSi, Phys. Rev. Lett. **110**, 066601 (2013).

[51] A. Barry, J. M. D. Coey, L. Ranno, and K. Ounadjela, Evidence for a gap in the excitation spectrum of CrO_2, J. Appl. Phys. **83**, 7166 (1998).

[52] Y. Xu, J. Zhang, G. Cao, C. Jing, and S. Cao, Low-temperature resistivity minimum and weak spin disorder of polycrystalline $La_{2/3}Ca_{1/3}MnO_3$ in a magnetic field, Phys. Rev. B **73**, 224410 (2006).

[53] D. Rani, J. Kangsabanik, K. G. Suresh, N. Patra, D. Bhattacharyya, S. N. Jha, and A. Alam, Origin of Local Atomic Order and Disorder in $Co_2Fe_{1-x}Cr_xSi$ Heusler Alloys: Theory and Experiment, Phys. Rev. Appl. **10**, 054022 (2018).

[54] J. P. Heremans, V. Jovovic, E. S. Toberer, A. Saramat, K. Kurosaki, A. Charoenphakdee, S. Yamanaka, and G. J. Snyder, Enhancement of thermoelectric efficiency in PbTe by distortion of the electronic density of states, Science **321**, 554 (2008).

[55] P. Mandal, Temperature and doping dependence of the thermopower in $LaMnO_3$, Phys. Rev. B **61**, 14675 (2000).

[56] J. Yang, Y. P. Sun, W. H. Song, and Y. P. Lee, Thermopower and thermal conductivity of the electron-doped manganite $La_{0.9}Te_{0.1}MnO_3$, J. Appl. Phys. **100**, 123701 (2006).

[57] A. Banerjee, S. Pal, S. Bhattacharya, B. K. Chaudhuri, and H. D. Yang, Magnetoresistance and magnetothermoelectric power of $La_{0.5}Pb_{0.5}Mn_{1-x}Cr_xO_3$, Phys. Rev. B **64**, 104428 (2001).

[58] R. Das, A. Chanda, and R. Mahendiran, Influence of magnetic field on electrical and thermal transport in the hole doped ferromagnetic manganite: $La_{0.9}Na_{0.1}MnO_3$, RSC Adv. **9**, 1726 (2019).

[59] J. Holanda, O. A. Santos, R. O. Cunha, J. B. S. Mendes, R. L. Rodríguez-Suárez, A. Azevedo, and S. M. Rezende, Longitudinal spin Seebeck effect in permalloy separated from the anomalous Nernst effect: Theory and experiment, Phys. Rev. B **95**, 214421 (2017).

[60] D. Kan and Y. Shimakawa, Strain effect on thermoelectric properties of $SrRuO_3$ epitaxial thin films, Appl. Phys. Lett. **115**, 22403 (2019).

[61] N. F. Mott, H. Jones, H. Jones, and H. Jones, *The Theory of the Properties of Metals and Alloys* (Courier Dover Publications, New York, 1958).

[62] N. Nagaosa, J. Sinova, S. Onoda, A. H. MacDonald, and N. P. Ong, Anomalous Hall effect, Rev. Mod. Phys. **82**, 1539 (2010).